Cyto- and bio-compatibility assessment of plasma-treated PVDF scaffolds for cardiac tissue engineering

Maria Kitsara1*, Gaëlle Revet1, Jean-Sébastien Vartanian-Grimaldi1, Alexandre Simon1, Mathilde Minguy1, Antoine Miche2, Vincent Humblot2,3, Thierry Dufour4*† and Onnik Agbulut1*†

1UMR CNRS 8256, INSERM ERL 1164, Biological Adaptation and Ageing, Institut de Biologie Paris-Seine, Sorbonne Université, Paris, France,
2UMR CNRS 7197, Laboratoire de Réactivité de Surface, Sorbonne, Université, Paris, France,
3UMR 6174 CNRS, FEMTO-ST Institute, Université Bourgogne Franche-, Comté, Besançon, France,

Summary

As part of applications dealing with cardiovascular tissue engineering, drop-cast PVDF scaffolds have been treated by cold plasma to enhance their adherence to cardiac cells. The scaffolds were treated in a dielectric barrier device where cold plasma was generated in a gaseous environment combining a carrier gas (helium or argon) with/without a reactive gas (molecular nitrogen). We show that an Ar-N_2 plasma treatment of 10 min drives significant hydrophilization of the scaffolds, with contact angles as low as 52.4° instead of 132.2° for native scaffolds. Correlating optical emission spectroscopy to X-ray photoelectron spectroscopy shows that O and OH radicals from the plasma phase can functionalize the surface scaffolds, hence a better wettability. For all plasma-treated PVDF scaffolds, the viability of primary cardiomyocytes is increased, showing a well-organized sarcomeric structure (α-actinin immunostaining). The efficacy of plasma treatment has also been supported by real-time PCR analysis to demonstrate an increased expression of the genes related to adhesion and cardiomyocyte function. Finally, the biocompatibility of the PVDF scaffolds has been studied in a cardiac environment, after implantation of acellular scaffolds on the surface of the heart of healthy mice. Seven days after implantation, no exuberant fibrosis and no multinucleated giant cells were visible in the grafted area, hence demonstrating the absence of a foreign body reaction and the perfect biocompatibility of these scaffolds.

1. Introduction

The objective of cardiovascular tissue engineering (CTE) is to develop therapeutic options for structural, functional and vascular heart diseases, especially through the innovation of contractile tissues that can replace missing or damaged myocardial tissues. Among the various CTE strategies investigated so far, biomaterials and scaffolds represent a major component either alone or combined with cells and/or bioactive molecules [Camman, 2021], [Kitsara, 2022].

Poly(vinylidene fluoride) (PVDF) is a thermoplastic semi-crystalline polymer which, in more of being cheap and easy-to-process, exhibits attractive electroactive properties. Depending on its macromolecular chain conformations, it can crystallize into five different types of phases, where α, β and γ are the most important: α is non-polar, while β and γ are polar [Fakhri, 2016]. Since α remains the most common form of PVDF, several processes have already been explored to transform this non-polar phase into polar ones. Among these processes, one can cite mechanical stretching, polarization and electrospinning [Deng, 2020], [Li, 2022], [Angel, 2022], [Song, 2022], [Kitsara, 2017], [Yuan, 2022], [Kitsara, 2015].

In tissues transmitting electrical signals, such as the cardiac muscle, PVDF appears as a promising scaffold candidate. PVDF scaffolds have not been explored up to now for cardiac tissue engineering, except for two studies using the copolymer PVDF-TrFE [Hitscherich, 2016], [Adadi, 2020]. Here, we propose to use PVDF scaffolds fabricated by drop casting, because of the ease and low cost of the method as it does not require special equipment.

In our previous study, we have shown that drop-cast PVDF scaffolds consist of globular particles interconnected with thin nanofibrils that form a structure of high porosity [Kitsara, 2019]. The globular structure was reported for samples that were dissolved in DMF [Gregorio, 1999], while the co-presence of a solvent of low boiling point such as acetone, aided in the pores formation due to its high evaporation rate. Regarding the piezoelectricity, we have proven with XRD and FTIR analyses that the scaffolds fabricated by drop-casting exhibited piezoelectric properties, although mainly attributed to the γ phase. It was concluded that drying of the drop-cast scaffolds at room temperature under a fume hood, which accelerated the solvent evaporation, and taking into account the higher proportion of the volatile acetone over DMF in the final solution, led to the transition of α to γ phase, and to β phase in a lesser extent [Kitsara, 2019]. Now that the polarization of PVDF under its γ phase is mastered according to the above described process, it is essential to address the following issue: PVDF is a hydrophobic polymer that does not allow adequate wetting, and subsequently satisfactory adhesion of cells on its surface [Dufour, 2013], [Lech, 2020].

In this study, we propose the treatment of drop-cast PVDF scaffolds using an atmospheric pressure plasma process supplied with various gas mixtures. Hence the chemical surface properties of the drop-cast PVDF scaffolds can be tailored with the aim to enhance the adhesion of cardiac cells. The various plasma-treated scaffolds were cellularized with cardiomyocytes derived from neonatal rat hearts. Cardiomyocytes structural analysis indicated the optimum plasma treatment conditions of PVDF that can be applied for cardiac tissue engineering. Further, the biocompatibility of plasma-treatd PVDF scaffolds has been assessed in a cardiac environment by implanting acellular PVDF scaffolds in the hearts of healthy mice.

2. Experimental Section

2.1. Preparation of the PVDF scaffolds

PVDF powder (M.W. 534 K), DMF and acetone were purchased from Sigma-Aldrich. PVDF solutions of 3% w/v and 5% w/v in DMF/acetone (40/60) were prepared by simultaneously agitating and heating at 60 °C for at least 2 hours. Then a drop of each solution was deposited on glass lamella of 13mm diameter. The drop-cast scaffolds were let to dry under a fume hood for 2 days at room temperature.

2.2. Scaffolds treatment with atmospheric plasma

The scaffolds were exposed to micro-discharges of cold plasma in a dielectric barrier device (DBD) operating at atmospheric pressure. This device comprises a quartz tube showing a rectangular section of 30 mm by 10 mm with a length of 30 cm. It is completed with two electrodes 10 cm long: an electrode polarized to high voltage (sine, 8 kV, 600 Hz) and a counter-electrode connected to a capacitor (100 pF) that is connected to the ground, as sketched in Figure 1. The area of the interelectrode gap was large enough to simultaneously treat 6 scaffolds. The DBD was supplied with a carrier gas (helium or argon) at a flow rate of 2 slm with/without reactive gas (molecular nitrogen) on a range between 0 and 20 sccm. All plasma treatments were operated during 10 min.

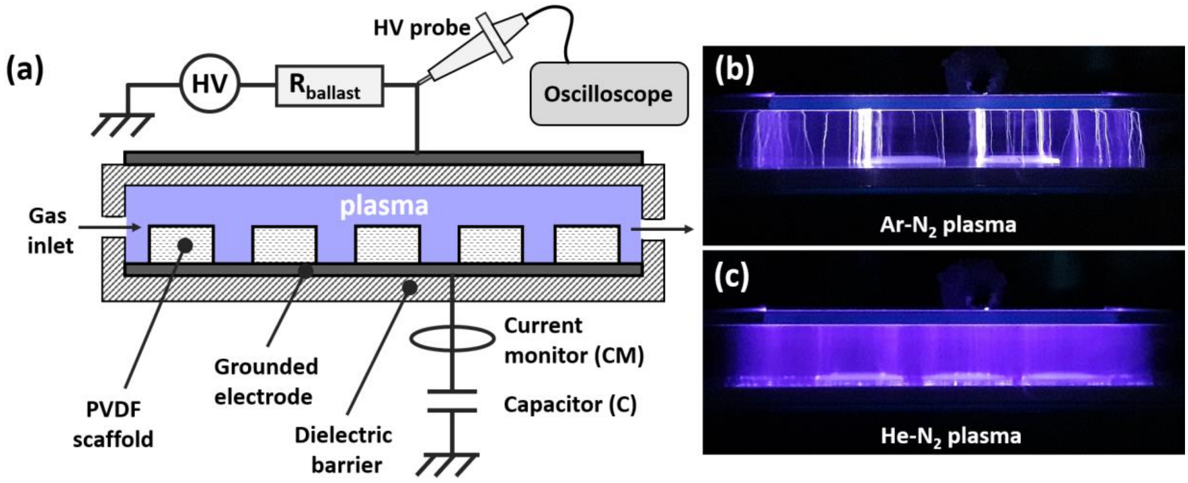

Figure 1. Dielectric barrier device (DBD) set up. *(a) Schematic representation of the DBD. Images during operation of (b) Ar-N$_2$ plasma discharge and (c) He-N$_2$ plasma.*

2.3. Plasma diagnostics

The plasma phase was analyzed using an optical emission spectrometer (SR-750-B1-R model from Andor company) equipped with an ICCD camera (Istar DH340T model from Andor company). The spectrometer operated in the Czerny Turner configuration with a focal length of 750 mm while diffraction was achieved with a 1200 grooves.mm^{-1} grating in the visible range. The following parameters were selected for all experiments: intensification factor = 4000, exposure time = 50 ms, number of accumulations = 200. Electrical measurements were carried out using an analog oscilloscope (Wavesurfer 3054, Teledyne LeCroy), a high voltage probe (Tektronix P6015A 1000:1) and a current monitor (Pearson, 2877), as sketched in Figure 1. Plasma electrical power was measured by plotting the Lissajous curve of the DBD [Dufour, 2021]. A current transformer (Pearson company, model 2877) is also utilized to characterize the distribution of the micro-discharges.

2.4. Scaffolds' surface characterization

Scanning electron microscope (SEM) was used to visualize the structure of the scaffolds using the system Gemini SEM 500 from Zeiss. The samples were sputtered with a thin platinum layer prior to SEM observation using a high vacuum sputter coater (ACE600, Leica). Images at different magnifications were obtained on at least five different areas in the same sample and in three different samples with the same conditions. The images were performed by applying a beam voltage of 3 kV and using InLens detector.

Water contact angle (WCA) measurements were performed using the DSA 30 system from Krüss. The measurements were achieved at room temperature (20 °C) following the Sessile drop method. The volume of the applied drops of deionized water was 1 µL and the WCA were measured 10 seconds after drop deposition. WCA data were obtained by averaging over at least three measurements in different areas on the samples surface.

X-ray photoelectron spectroscopy (XPS) analyses were performed using an Omicron Argus X-ray photoelectron spectrometer, equipped with a monochromated AlK$_\alpha$ radiation source ($h\nu$ = 1486.6 eV) and a 300 W electron beam power. The emission of photoelectrons from the sample was analyzed at a takeoff angle of 90° under ultra-high vacuum conditions ($\leq 10^{-10}$ Torr). Spectra were carried out with a 100 eV pass energy for the survey scan and 20 eV pass energy for the C 1s, O 1s, N 1s and S 2p regions. Binding energies were calibrated against the Au 4f$_{7/2}$ binding energy at 84.0 eV and element peak intensities were corrected by Scofield factors [Scoffield, 1976]. The peak areas were determined after subtraction of a linear background. The spectra were fitted using Casa XPS v.2.3.15 software (Casa Software Ltd., U.K.) and applying a Gaussian/Lorentzian ratio G/L equal to 70/30.

2.5. Isolation of neonatal rat cardiomyocytes and cell culture

Newborn rat primary cardiomyocytes were obtained from 1-day-old Wistar RjHan rat (Janvier Labs, Saint-Berthevin, France). The hearts were cut in small pieces and the cardiac cells were isolated, using a neonatal heart dissociation kit (Miltenyi Biotec, Paris, France) according to the manufacturer's instructions. Cardiomyocytes were purified by depletion of non-target cells (such as fibroblasts, endothelial cells, blood cells) using a neonatal cardiomyocyte isolation kit (Miltenyi Biotec, Paris, France). 5 x 10^5 cardiomyocytes were seeded on each PVDF scaffold mounted in a CellCrown™ (Scaffdex, Tampere, Finland) in a 48-well plate and cultured with DMEM medium (with 4.5g/L D-Glucose and without Na Pyruvate) supplemented with L-glutamine, penicillin-streptomycin, 10% horse serum and 5% foetal bovine serum at 37 °C and 5% CO_2 for 3 days. All animal studies were approved by our institutional Ethics Committee "Charles Darwin" and conducted according to the French and European laws, directives, and regulations on animal care (European Commission Directive 2010/ 63/EU) under the license C75.05.24.

2.6. Immunostaining and morphology analysis of primary cardiomyocytes

The primary cardiomyocytes were washed with PBS and fixed with 4% paraformaldehyde solution. After 3 washing steps, they were incubated with 5% bovine serum albumin (BSA) for 1 hour. Then, the cells were incubated for 90 minutes at room temperature with antibodies against α-actinin (mouse IgG, dilution 1:300, Sigma-Aldrich, Saint-Quentin-Fallavier, France). After 3 washes in PBS, primary cardiomyocytes were incubated in the presence of the secondary antibody (Alexa 488 goat-anti-mouse, dilution 1:1000; Life Technologies). The scaffolds were mounted with mowiol containing 5 µg/ml Hoescht 33342 (Life Technologies). Images were captured using a motorized confocal laser scanning microscope (Leica TCS SP5). Cardiomyocyte surface area and perimeter, cardiomyocyte length-to-width ratio and roundness index were measured using ImageJ software as described in [Flaig, 2020].

2.7. Relative quantification of gene expression by real-time PCR

Total RNA was extracted from the primary cardiomyocytes using TRIzol® (Thermo Fisher Scientific, Saint-Herblain, France) following the manufacturer's instructions. From 500 ng of extracted RNA, the first-strand cDNA was then synthesized using a RevertAid First Strand cDNA Synthesis Kit (Thermo Fisher Scientific, Saint-Herblain, France) with random hexamers according to the manufacturer's instructions. Using the Light Cycler® 480 system (Roche Diagnostics), the reaction was carried out in duplicate for each sample in a 6 µL reaction volume containing 3 µL of SYBR Green Master Mix, 500 nM of the forward and reverse primers each and 3 µL of diluted (1:25) cDNA. The thermal profile for the SYBR Green qPCR was 95 °C for 8 min, followed by 40 cycles at 95 °C for 15 s, 60 °C for 15 s and 72 °C for 30 s. To exclude PCR products amplified from genomic DNA, primers were designed, when possible, to span one exon-exon junction. The mean gene expression stability of 3 genes, Actb (hydroxymethylbilane synthase), B2M (beta-2-microgobulin) and Nubp1, were used as the reference transcripts. Data were collected and analyzed using the LightCycler® 480 software release 1.5.0 (Roche Diagnostics).

Assessment of cardiac and adhesion index were constructed using the fold change relative to control in quantitative PCR-based expression of α-actinin (*Actn1*), myosin heavy chain 7 (*Myh7*), phospholamban (Pln), ATPase Sarcoplasmic/Endoplasmic Reticulum Ca2+ Transporting 2 (*Atp2a2*) and alphaB-crystallin (*Cryab*) for cardiac index and the fold change relative to control in quantitative PCR-based expression of cadherin-2 (*Cdh2*), cadherin-13 (*Cdh13*), collagen-type 1-alpha 1 (*Col1a1*), extracellular matrix protein1 (*Ecm1*), elastin (*Eln*), laminin subunit alpha 4 (*Lama4*), laminin subunit beta 2 (*Lamb2*) and laminin subunit gamma 1 (*Lamc1*) for adhesion index. The control (non-treated surface) value is set at 1.0.

2.8. Epicardial grafting in mice

Thirty-seven 8-week-old female Swiss mice (Janvier Labs, Saint-Berthevin, France) were used for the bio-compatibility assessment. All procedures were performed in accordance with national and European legislations, in conformity with the Public Health Service Policy on Human Care and Use of Laboratory Animals under the license A751320. All animal studies were approved by our institutional Ethics Committee "Charles Darwin" (Permit number: 4370) and conducted according to the French and European laws, directives, and regulations on animal care (European Commission Directive 86/609/EEC). All animals underwent a left lateral thoracotomy after intraperitoneal ketamine (100 mg/kg; Merial, France)-xylazin (10 mg/kg; Bayer, France) anesthesia and tracheal ventilation. Analgesia was performed for 2 days after surgery with a 2 mg/kg intraperitoneal injection of profenid® (Merial). Acellular PVDF scaffolds were sutured (surface approximately 60 mm^2) on the surface of the ventricle of the mice. The animals were sacrificed 7 and 28 days after implantation to assess the biocompatibility of the scaffolds by cervical dislocation. After sacrifice, hearts were removed and weighted.

2.9. Tissue processing and histological analysis

For histological analysis, the ventricles were separated in two halves by a short-axis section through the midportion of the heart. The upper part was immediately fixed in 4% of formaldehyde for 24 h, dehydrated, and embedded in paraffin and lower part were snap frozen in liquid nitrogen immediately after dissection. 10 µm heart sections were made using a microtome (Leica Microsystems, Nanterre, France), stained with hematoxylin and eosin for visualization of general morphology, mounted in Eukitt (CML, France) and examined by light microscopy. Images were taken with a microscope (Leica Microsystems, Nanterre, France) equipped with a digital camera. At least 5 animals were used for each experimental point.

2.10. Statistical analyses

Analyses were conducted using GraphPad Prism 7.00 (GraphPad Software Inc., SD, USA). For one- way analysis of variance, the normality was checked using the Shapiro-Wilk normality test. If the normality of distribution assumption was not met, the nonparametric Mann-Whitney test was used instead of ANOVA. If a significant difference was found, then multiple comparison tests were performed to compare the different groups analyzed (Dunn's or Holm-Sidak's multiple comparison test following a nonparametric or parametric test, respectively). A *p*-value ≤ 0.05 was considered significant. Values are given as the means ± standard error of the mean (SEM).

3. Results and Discussion

3.1 Plasma phase characterization

The scaffolds were treated by DBD supplied in helium or argon (carrier gas) at 2 slm mixed with molecular nitrogen (reactive gas) for flow rates comprised between 0 and 100 sccm. Figure 2a shows the variations of plasma current and voltage as a function of time. While the voltage profiles remain close to the ones to the others, the current profiles strongly depend on the gas mixture. The amplitude of the current peaks remains in the range of 0.5 A to 2.0 A when argon is used as carrier gas while it falls to values between 5 mA and 40 mA if helium is injected instead. In both cases, increasing the flow of N_2 significantly increases the amplitude of the current peaks. Also, it should be noted that the overall number of current peaks is always lower with argon (typically a dozen per period) than with helium (typically 60-80 peaks per period) and that an increase in N_2 flow rate systematically raises this number. Knowing I_{pl} and V_{pl} in the setup described in section 2.3, it is possible to assess the plasma power. The Figures 2b and 2c represent Lissajous diagrams of the 4 conditions introduced in Figure 2a, i.e. the overall charge of plasma (Q_{pl}) as a function of plasma voltage (V_{pl}). It turns out that whatever the gas mixtures performed in this work, the electrical power delivered to the DBD remains always close to 1.3 W (± 0.1 W).

Cold atmospheric plasma performed in dielectric barrier devices correspond to micro-discharges which follow one another over extremely short times (<10 µs). While the plasma is filamentary with argon (figure 1b), it appears more diffuse with helium (figure 1c), thus showing the impact of the nature of the carrier gas on the spatial and temporal distribution of the micro-discharges. Even if plasma power remains close to 1.3 W in all gas mixtures, one can reasonably expect populations of micro-discharges showing different energy profiles depending on the gas supply. The Figure 2d reports the average energy per micro-discharge (⌊) for argon or helium with/without molecular nitrogen. The value of ⌊ is close to 100 µJ in pure argon while it only raises 25 µJ for pure helium. Then, increasing N_2 flow rate from 0 to 100 sccm is accompanied with a gradual increase of ⌊ with values of 100 µJ and 500 µJ for He-N_2 plasmas and Ar-N_2 plasma respectively. These micro-discharges interplay with the gaseous environment to produce active species but also impinge on the scaffolds. In consequence, even if Ar-N_2 and He-N_2 plasmas can drive the production of active species in similar levels, their effects on the scaffolds can strongly differ.

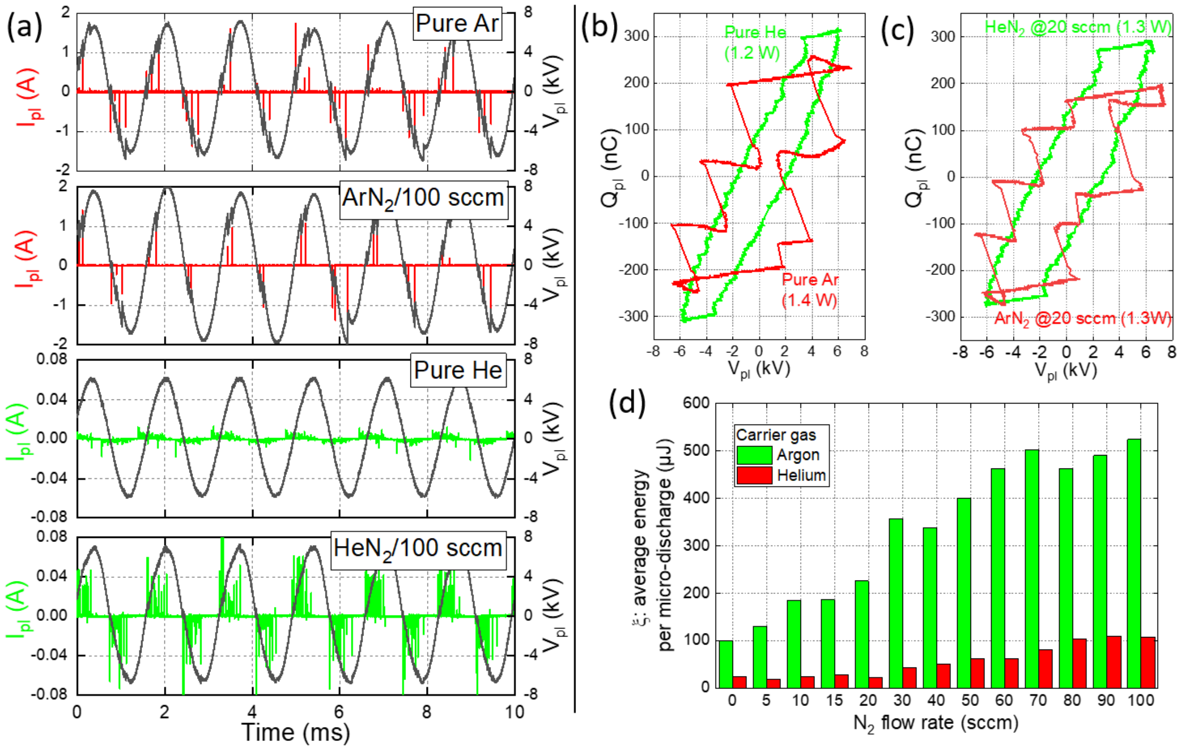

Figure 2. Electrical characterizations of plasma dielectric discharges supplied in argon or helium (2 slm) with/without molecular nitrogen (0-100 sccm)*. (a) time profiles of plasma voltage and plasma current (b, c) Lissajous diagrams to assess plasma power, (d) Average energy per micro-discharge.*

The intensity of the radiative species in He-N_2 and Ar-N_2 plasmas has been quantified using optical emission spectroscopy. The Figure 3 reports the relative intensities of Ar ($2p_{1/2} - 2p_{3/2}$), He ($3S_1 - 3P_1$), OH ($A^2\Sigma^+ - X^2\Pi$), O ($5P_{3,2,1} - 5S_2$), N_2 ($c^3\Pi_u - b^3\Pi_g$) and N_2^+ ($B^2\Sigma_u^+ - X^2\Sigma_g^+$) as a function of the N_2 flow rate. In the case of the Ar-N_2 plasma, only molecular nitrogen is excited. At atmospheric pressure, the formation of N_2^+ ions through Penning ionization with metasble argon species is not possible, their energy not being sufficiently high. The production of the OH radicals as a function N_2 flow rate result from the more effective dissociation of water molecules. In the He-N_2 plasma, the production of N_2 and OH species are similar to those observed in the previous case, although the intensities measured here are slightly higher. The main difference resulting from the utilization of helium as carrier gas is the production of N_2^+ through Penning ionization with the high-energetic He metastable species.

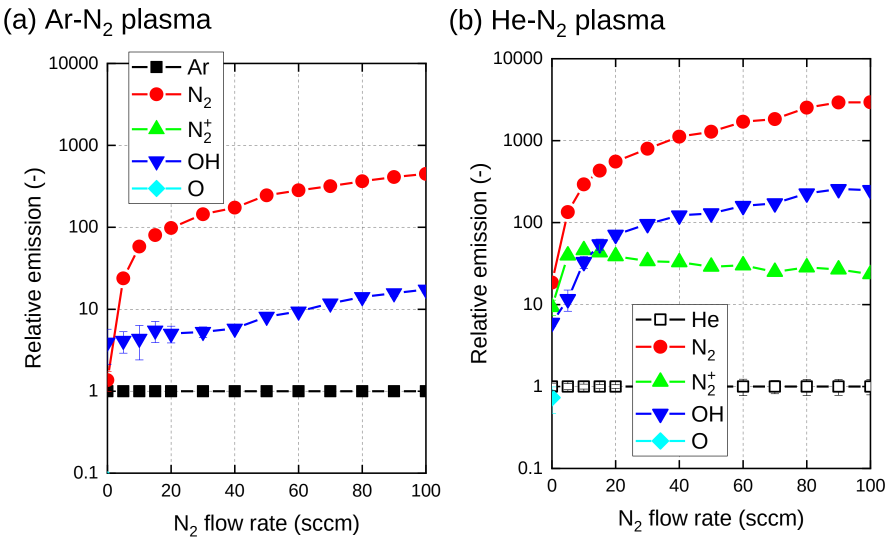

Figure 3. Optical emission spectra of plasma generated in carrier gas at 2 slm (argon or helium) mixed with molecular nitrogen comprised between 0 and 100 sccm. *(a) Ar-N_2 plasma and (b) He-N_2 plasma.*

3.2 Morphology of drop-cast scaffolds

The drop-cast PVDF scaffolds demonstrate a highly porous morphology, as indicated by SEM (Figure 4). These results are consistent with the previous findings, regarding the globular morphology of the scaffolds and their high porosity that is necessary for tissue engineering [Kitsara, 2019]. The thinner scaffolds obtained from 3%PVDF were not easily manipulated for grafting, therefore the thicker one (5%PVDF) were utilized for the physicochemical and biological studies. Figures c, d indicate that the morphology of the scaffold has not been affected by the drop casting process and both sides are the same, which gives flexibility in the process of grafting (no special care for marking the sides is required).

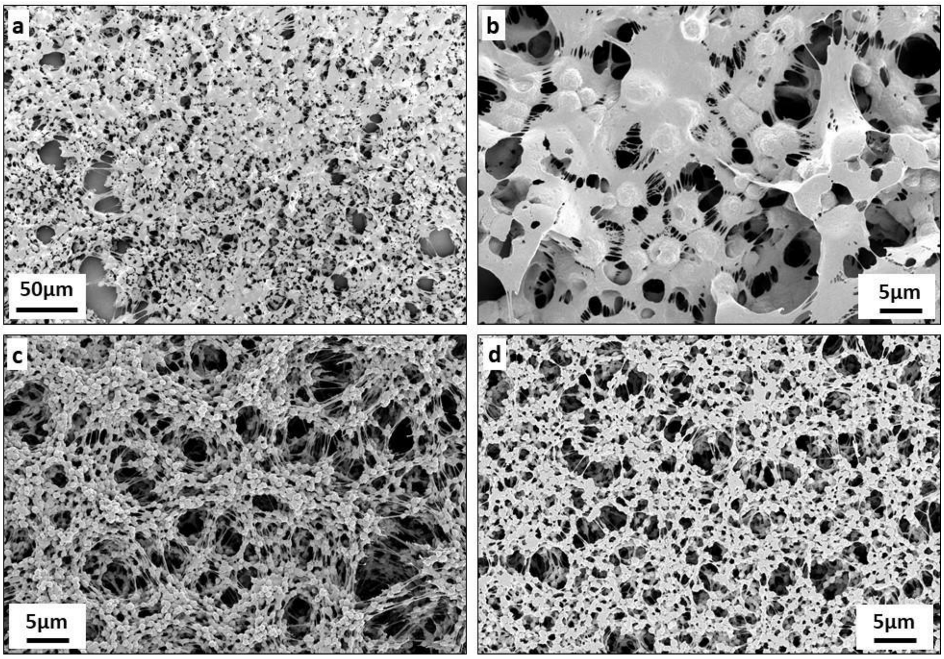

***Figure 4. Scanning electron microscope (SEM) images of drop-cast scaffolds**: (a), (b) Thin PVDF obtained by 3% w/v solution. (c), (d) Thick PVDF obtained by 5% w/v solution. The images (a), (b), (c) correspond to the top side of the scaffold, while (d) shows the bottom side that is in contact with the lamella.*

3.2 Surface functionalization of PVDF scaffolds: effect of plasma treatment

Regardless of the plasma treatment (He or Ar with/without N_2 gas mixture), the PVDF surface became hydrophilic, as shown in Figure 5 which reports the shape profiles of the deposited drops as well as the corresponding water contact angles (WCA) values. While the native surface of PVDF scaffold had a WCA as high as 132.2°, values as low as 52.4° and even 17.3° were obtained for Ar(N_2) plasma and He(N_2) respectively. These WCA values can be correlated with the production of OH radicals within the plasma phase as evidenced by optical emission spectroscopy in Figure 3. Unsurprisingly, the most hydrophilic states correspond to the highest emissions of OH radicals. This gain in hydrophilicity can be correlated with XPS analyses performed on the carbon C 1s and fluorine F 1s regions. The C 1s high binding energy contributions (290 eV assigned to -CF2 moieties) decrease together with the F 1s signal, as reported in Table 1. New C 1s contributions appear around 288 eV that can be assigned to CFO groups. As evidenced in the XPS spectra in Figure 5, these contributions correspond to -$\underline{C}$-C=O(OH) and -CF$\underline{O}$-CH_2- for a binding energy of 288.5 eV and to -CF_2-$\underline{C}$HO- and -CF_2-$\underline{COOH}$ at 287.1 eV. Concentrations of the carbon bonds related to C 1s, the oxygen bonds related to O 1s and the CF_2 bond related to F 1s for PVDF scaffolds . This is also verified on the oxygen O 1s signal with increased intensities and contributions shifts towards higher binding energies that correlated with the hydrophilicity changes (WCA analysis).

Condition	Control	Pure Ar	ArN_2	Pure He	HeN_2
Drop profile	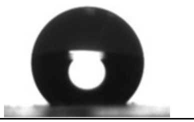	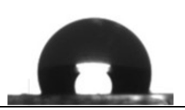			
WCA (°)	132.2° (± 2.1°)	115.8° (± 2.4°)	52.4° (± 1.3°)	44.1° (± 2.3°)	17.3° (± 2.9°)

Figure 5. WCA measurements on plasma-treated PVDF scaffolds.

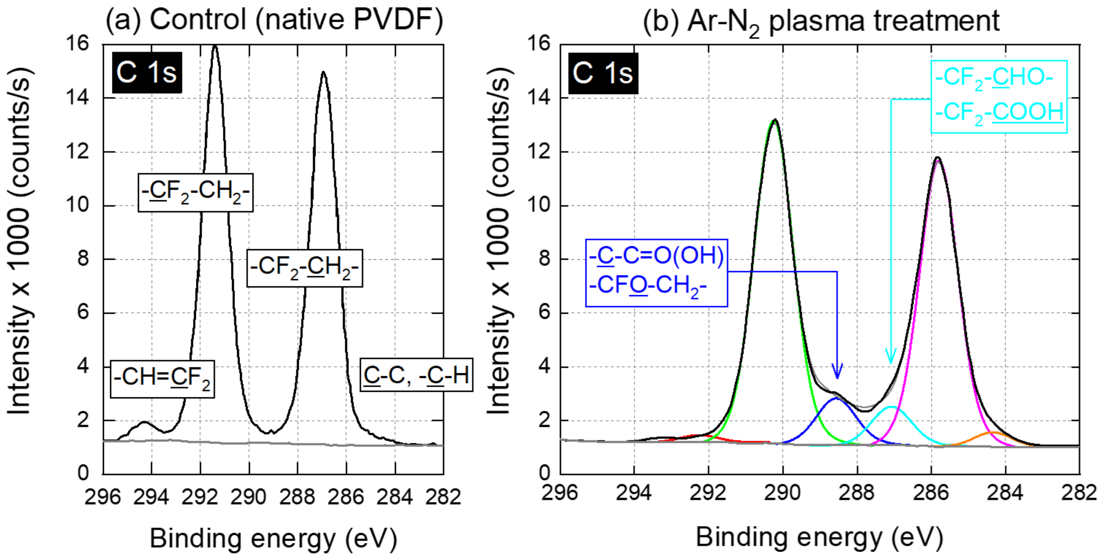

Figure 6. C 1s high resolution XPS spectra of (a) untreated PVDF and (b) PVDF treated with Ar-N_2 plasma (Φ_{N2} = 20 sccm).

Condition	**Φ_{N2} (sccm)**	**Surface atomic composition**			**Atomic Ratio**	
		C 1s	**F 1s**	**O 1s**	**F/C**	**O/C**
No treatment (Native PVDF)	-	61.7%	35.7%	2.1%	0.58	0.03
After Ar(N_2) plasma exposure	0	52.5%	37.4%	10.1%	0.71	0.19
	20	51.2%	40.0%	8.8%	0.78	0.17
After He(N_2) plasma exposure	0	51.3%	40.9%	7.8%	0.80	0.15
	20	51.1%	40.1%	8.8%	0.78	0.17

Table 1. Chemical surface composition of PVDF scaffolds without/with plasma treatment

Condi-tion	**Φ_{N2} (sccm)**	**C 1s**						**O 1s**		**F 1s**
		$-CH=\underline{C}F_2$	$-\underline{C}F_2-CH_2-$	$-\underline{C}-C=O(OH)$ $-CF\underline{O}-CH_2-$	$-CF_2-\underline{C}HO-$ $-CF_2-\underline{COOH}$	$-CF_2-\underline{C}H_2-$	$-\underline{C}-C, -\underline{C}-H$	$-C=\underline{O}(OH)$ $-CF_2-CH\underline{O}-$ $-CF\underline{O}-CH_2-$	$-C=O(\underline{O}H)$	$-CF_2-$
Native PVDF	-	(292.1 eV) 3.5%	(290.2 eV) 45.9%	(288.5 eV) 0.5%	(287.1 eV) 0.3%	(285.6 eV) 42.6%	(284.4 eV) 1.1%	(532.5 eV) 0.6%	(533.8 eV) 0.8%	(687.4 eV) 4.7%
PVDF after Ar(N_2) plasma exposure	0	(292.1 eV) 0.8%	(290.2 eV) 21.2%	(288.4 eV) 4.2%	(287.2 eV) 4.2%	(285.5 eV) 21.7%	(284.4 eV) 0.8%	(532.5 eV) 5.4%	(533.8 eV) 4.8%	(687.4 eV) 36.9%
	20	(291.9 eV) 0.4%	(290.2 eV) 23.5%	(288.5 eV) 3.1%	(287.0 eV) 2.8%	(285.7 eV) 20.4%	(284.4 eV) 1.4%	(532.4 eV) 4.3%	(533.7 eV) 4.6%	(687.4 eV) 39.6%
PVDF after He(N_2) plasma exposure	0	(292.1 eV) 0.6%	(290.3 eV) 23.2%	(288.6 eV) 2.4%	(287.2 eV) 2.5%	(285.9 eV) 21.5%	(284.5 eV) 1.3%	(532.6 eV) 3.9%	(533.9 eV) 3.9%	(687.5 eV) 40.7%
	20	(292.3 eV) 0.5%	(290.3 eV) 23.1%	(288.6 eV) 3.3%	(287.1 eV) 2.8%	(285.8 eV) 20.5%	(284.3 eV) 1.1%	(532.4 eV) 5.0%	(533.8 eV) 4.1%	(687.3 eV) 39.6%

Table 2. Concentrations of the carbon bonds related to C 1s, the oxygen bonds related to O 1s and the CF_2 bond related to F 1s for PVDF scaffolds before/after plasma treatments. Concentrations are expressed in %. Values in parenthesis correspond to the binding energies expressed in eV.

3.3 Surface functionalization and cardiomyocytes survival: morphological analysis

The culture of primary cardiomyocytes for 6 days indicated a significant increase of the viable cells on all plasma-treated scaffolds in comparison to the non-treated PVDF. As shown in Figure 7a, fluorescence microscopy reveals that only few cardiomyocytes survived on the non-treated PVDF, which created agglomerates. On the contrary, the cardiomyocytes upon culture on all the plasma-treated PVDF show a well-organized sarcomeric structure, as observed by α-actinin immunostaining (From figure 7b to 7f). Our results show that cardiomyocytes can easily adhere and spread on the

PVDF scaffolds, with no apparent difference between all the plasma treatments achieved as part of this research work.

To determine the ability of newborn rat primary cardiomyocytes to grow on non-treated and plasma-treated PVDF scaffolds, we measured the following parameters: cardiomyocyte surface area, cardiomyocyte perimeter, cardiomyocyte length-to-width ratio and roundness index of the cardiomyocytes after 6 days of culture (Figure 7g). We notice an increase in the cardiomyocyte size (surface and perimeter), the cardiomyocyte length-to-width ratio of the cells on all plasma-treated PVDF in comparison to non-treated PVDF scaffolds after 6 days of culture. In contrast, we noticed a decrease of the roundness index of the cardiomyocytes cultured on plasma-treated PVDF. These findings suggest that cardiomyocytes can easily adhere and spread, as well as exhibit a physiological shape on plasma-treated PVDF scaffolds.

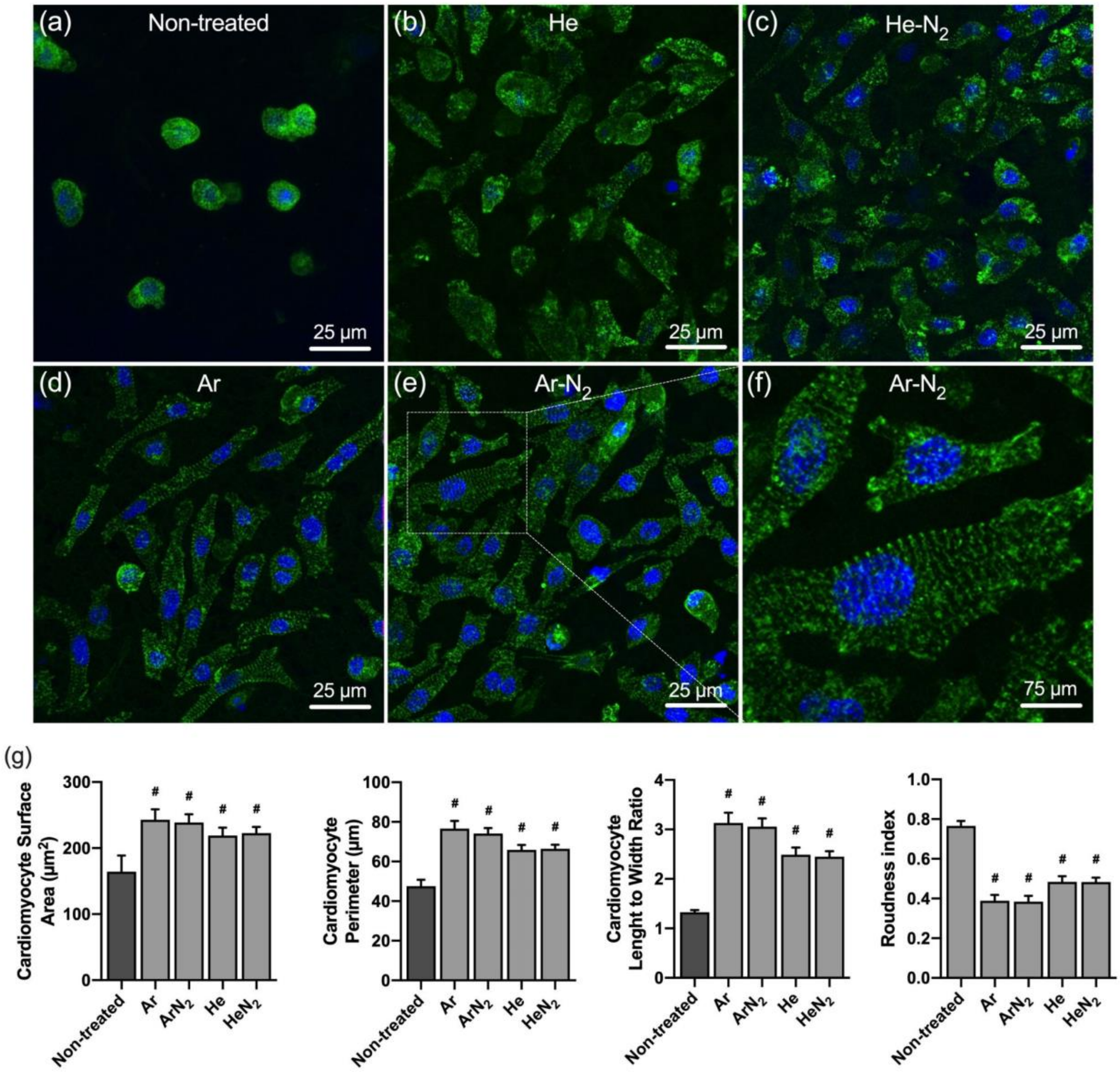

***Figure 7. Cellularization of the plasma-treated PVDF scaffolds with newborn rat primary cardiomyocytes**. Six days after cardiomyocytes seeding on non-treated PVDF (a), He plasma-treated (b); He-N_2 plasma-treated (c); Ar plasma-treated (d); Ar-N_2 plasma-treated PVDF (e-f), cardiomyocytes were immunolabeled with the antibody against α-actinin (green). Nuclei appear blue due to Hoescht 33342 staining. White dot lines in (e) show a higher-magnification area in (f). Cardiomyocyte surface area and perimeter, cardiomyocyte length-to-width ratio and roundness index were measured using ImageJ software (g). (n > 40 cardiomyocytes per condition). Values are given as means ± standard error of the mean. # indicates a significant difference compared to the non-treated PVDF scaffold.*

The efficacy of plasma treatment was also supported by real-time PCR analysis which demonstrated an increased expression of the genes related to adhesion and cardiomyocyte function. For a closer analysis, two following indexes, *i.e.* adhesion index and cardiac index were constructed using the fold change relative to control of mRNA expression of adhesion and cardiac function related genes, respectively. The adhesion index was constructed using cadherin-2, cadherin-13, collagen-type 1-α 1, extracellular matrix protein1, elastin, laminin subunit α 4, laminin subunit β 2 and laminin subunit γ 1 whereas the cardiac index was constructed using α-actinin, myosin heavy chain 7, phospholamban, ATPase, Sarcoplasmic/Endoplasmic Reticulum Ca^{2+} Transporting 2 (SERCA2) and α B-crystallin between the cardiomyocytes cultured on plasma-treated vs non-treated PVDF. As shown in Figure 8a, whatever the plasma treatment, no significant difference is observed amongst the samples in terms of cell adhesion, although they all exhibit higher adhesion in comparison to the non-treated PVDF. It turns out that cell adhesion is not directly correlated with plasma-induced surface hydrophilization; this observation is consistent with the recent works of M. R. Alexander who pointed out that surface wettability measured by drop shape analysis is not always a relevant predictor of cell adhesion to scaffolds [Alexander, 2017]. For the genes related to the cardiomyocyte function, the cardiac index in cardiomyocytes cultured on ArN_2-treated surface is significantly higher compared to the other treatments, as clearly evidenced in Figure 8b. These results are in accordance with the immunofluorescence imaging. Interestingly, the Ar-N_2 plasma treatment differs from the three other ones by its ξ parameter, i.e. the average energy of the plasma micro-discharges. As reported in Figure 2c, the elevated values of $\xi_{Ar\text{-}N2}$ can be interpreted as micro-discharges transferring at local scale a stochastic distribution of micro heat channels. The contact points with the scaffold are transiently thermalized, resulting to a potential texturation and/or to the in-depth diffusion of the hydrophilic functions (hydroxyl, …), i.e. over depths that are beyond the WCA or XPS detectable ranges.

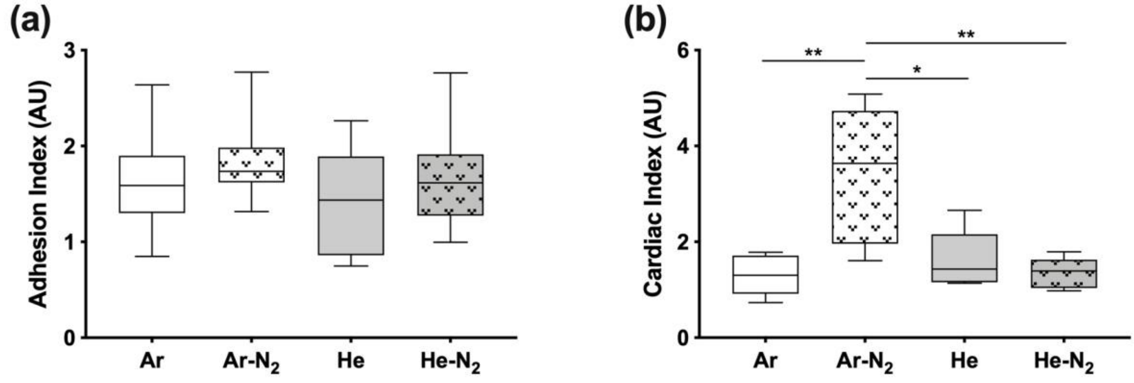

Figure 8. Boxplot representation of the adhesion and cardiac index. *(A) Adhesion index, (B) Cardiac index. The score was calculated using three independent experiments. The boxes represent the lower to upper quartile range, the error bars represent the entire range, the horizontal bar represents the median value. Non-treated surface values are set at 1.0.*

3.4 Biocompatibility of PVDF scaffolds assessed on murine models

The biocompatibility of the PVDF scaffolds was studied in a cardiac environment, after implantation of acellular scaffolds on the surface of the heart of healthy animals as previously described in our studies [Flaig, 2020], [Domengé, 2021], [Fiamingo, 2016], [Joanne, 2016]. We first evaluated the integrity of the scaffolds 7 days after implantation. As demonstrated in Figure 9, PVDF scaffolds were visible and well-integrated on the surface of the ventricle. No visible degradation of the scaffolds was observed in all conditions. After this evaluation, we focalized on the general morphology of grafted area. Seven days after implantation, in all conditions, no exuberant fibrosis and no multinucleated giant cells were visible in the grafted area. Only mononuclear cell infiltration was observed, hence demonstrating the absence of a foreign body reaction and the perfect biocompatibility of these scaffolds. It should be noted that we did not detect a significant difference between the plasma treated and non-treated PVDF scaffolds.

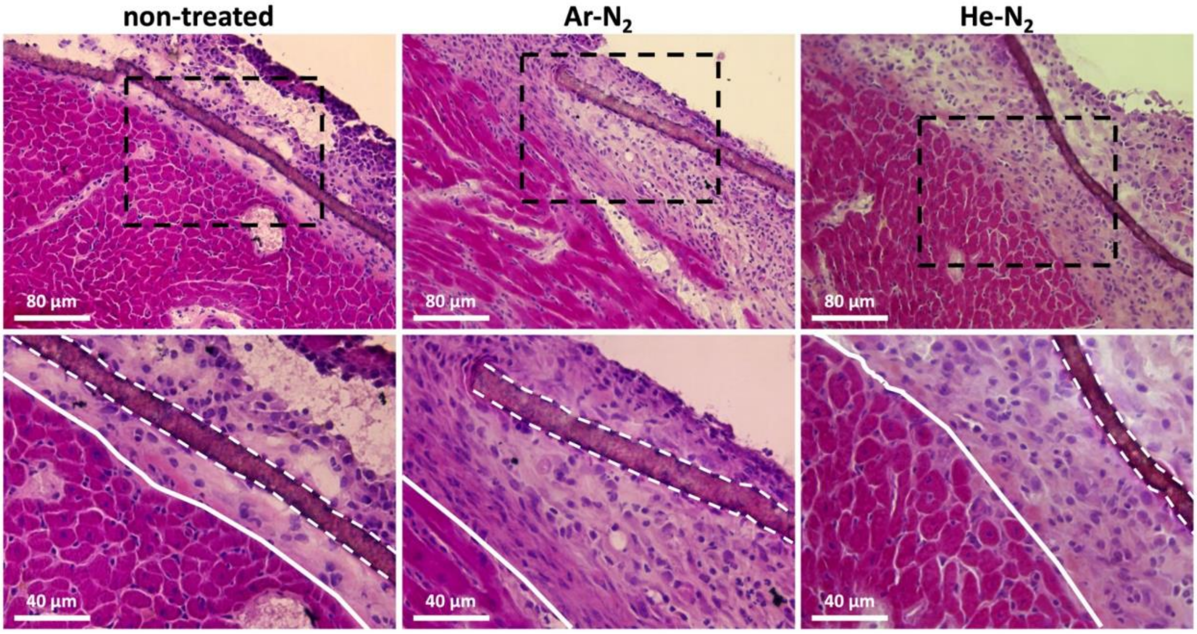

Figure 9. Biocompatibility of the PVDF scaffolds after implantation on the surface of the heart of healthy mice. *The residual scaffolds were visualized by hematoxylin-eosin staining after 7 days of implantation of non-treated, Ar-N_2 or He-N_2 treated PVDF dropcast scaffold. Black dashed framings (upper panel) show a higher magnification area (of the lower panel). White solid lines (lower panel) show the border between the grafted area and heart, while white dashed lines represent residual mats on the surface of the heart. Note the absence of multinucleated giant cells and exacerbated fibrosis in the grafted area.*

4. Conclusions

Our results indicate that plasma treatment can be efficient on PVDF scaffolds for improving cardiomyocytes viability and morphology. The changes in surface chemistry during the processing with plasma significantly enhanced cells adhesion and expansion. Amongst the different plasmas, Ar-N_2 led to the most efficient results and molecular analysis confirmed these findings. In addition, the biocompatibility study of plasma-treated PVDF scaffolds, upon implantation in mouse hearts indicated that PVDF scaffolds do not induce increased inflammation, proving for the first time that this material is a promising candidate for cardiac tissue engineering.

Acknowledgements

This work was supported by the LabEx REVIVE (ANR-10-LABX-73), and the Île-de-France Regional Council (DIM Respore). MK acknowledges personal funding from both LabEx REVIVE and DIM Respore too. The authors also acknowledge IMPC from Sorbonne University (Institut des Matériaux de Paris Centre, FR CNRS 2482) and the C'Nano projects of the Region Ile-de-France, for Omicron XPS apparatus funding. The authors also thank all of the personnel of the Animal Facility of the Sorbonne Université (UMS28, Paris-France); the Microscopy Platform (IBPS, Paris-France) for helpful advice and technical assis- tance during microscopy image acquisition and analysis.

References

[Fakhri, 2016] Improved electroactive phase content and dielectric properties of flexible PVDF nanocomposite films filled with Au- and Cu-doped graphene oxide hybrid nanofiller, Paris Fakhri, Haroon Mahmood, Babak Jaleh, Alessandro Pegoretti, Synthetic Metals, Volume 220, October 2016, Pages 653-660
https://doi.org/10.1016/j.synthmet.2016.08.008

[Kitsara, 2019] Permanently Hydrophilic, Piezoelectric PVDF Nanofibrous Scaffolds Promoting Unaided Electromechanical Stimulation on Osteoblasts, M. Kitsara; A. Blanquer, G. Murillo, V. Humblot, S. De Bragança Vieira, C. Nogués, E. Ibáñez, J. Esteve.; L. Barrios, *Nanoscale* **2019**, *11* (18), 8906-8917
https://doi.org/10.1039/C8NR10384D

[Gregorio, 1999] Gregorio Jr., R.; Ueno, E. M. Effect of Crystalline Phase, Orientation and Temperature on the Dielectric Properties of Poly (Vinylidene Fluoride) (PVDF). *J. Mater. Sci.* **1999**, *34* (18), 4489-4500
https://doi.org/10.1023/A:1004689205706

[Scoffield, 1976] Hartree-Slater Subshell Photoionization Cross-Sections at 1254 and 1487, J. H. Scofield, EV. *Journal of Electron Spectroscopy and Related Phenomena* **1976**, *8* (2), 129-137.

[Deng, 2020] Recent progress in tuning polymer oriented microstructures for enhanced thermoelectric performance, Liang Deng, Guangming Chen, Nano Energy, Volume 80, February 2021, 105448
https://doi.org/10.1016/j.nanoen.2020.105448

[Li, 2022] Polarization Mechanism Underlying Strongly Enhanced Dielectric Permittivity in Polymer Composites with Conductive Fillers, Bo Li, Clive A. Randall, Evangelos Manias, J. Phys. Chem. C., 2022, 126, 17, 7596-7604.
https://doi.org/10.1021/acs.jpcc.2c01592

[Angel, 2022] Recent advances in electrospinning of nanofibers from bio-based carbohydrate polymers and their applications, Nicole Angel, Songnan Li, Feng Yan, Lingyan Kong, Trends in Food Science & Technology, Volume 120, 2022, 308-324
https://doi.org/10.1016/j.tifs.2022.01.003

[Song, 2022] Electrospun 1D and 2D Carbon and Polyvinylidene Fluoride (PVDF) Piezoelectric Nanocomposites, Hang Song, Wenhui Song, Jin-hua Song, Virginia Martin Torrejon, Qinxiang Xia, Journal of Nanomaterials, vol. 2022, Article ID 9452318, 17 pages, 2022.
https://doi.org/10.1155/2022/9452318

[Yuan, 2022] Deep Eutectic Solvent - A Novel Additive to Induce Gamma Crystallization and Alpha-to-Gamma Phase Transition of PVDF, Muhua Yuan, Haijun Wang, Huihui Li, Chunlei Yuan, Tong Wang, Haibo Yang, Volume 223, Issue 4, 2022, 2100416 https://doi.org/10.1002/macp.202100416

[Adadi, 2020] Electrospun Fibrous PVDF-TrFe Scaffolds for Cardiac Tissue Engineering, Differentiation, and Maturation, Nofar Adadi, Moran Yadid, Idan Gal, Masha Asulin, Ron Feiner, Reuven Edri, Tal Dvir, Volume 5, Issue 3, 2020, 1900820 https://doi.org/10.1002/admt.201900820

[Hitscherich, 2016] The effect of PVDF-TrFE scaffolds on stem cell derived cardiovascular cells, Pamela Hitscherich, Siliang Wu, Richard Gordan, Lai-Hua Xie, Treena Arinzeh, Eun Jung Lee, Biotechnology & Bioengineering, Volume 113, Issue 7, 1577-1585, 2016 https://doi.org/10.1002/bit.25918

[Dufour, 2013] Competitive and synergistic effects between excimer VUV radiation and O radicals on the etching mechanisms of polyethylene and fluoropolymer surfaces treated by an atmospheric He–O2 post-discharge, T Dufour, J Hubert, N Vandencasteele, P Viville, R Lazzaroni, F Reniers, J. Phys. D: Appl. Phys. 46 (2013) 315203 (14pp) https://doi.org/10.1088/0022-3727/46/31/315203

[Lech, 2020] Surface modification of PLLA, PTFE and PVDF with extreme ultraviolet (EUV) to enhance cell adhesion, Adam Lech, Beata A. Butruk-Raszeja, Tomasz Ciach, Krystyna Lawniczak-Jablonska, Piotr Kuzmiuk, Andrzej Bartnik, Przemyslaw Wachulak, Henryk Fiedorowicz, Int. J. Mol. Sci. 2020, 21(24), 9679
https://doi.org/10.3390/ijms21249679

[Flaig, 2020] Design of Functional Electrospun Scaffolds Based on Poly(glycerol sebacate) Elastomer and Poly(lactic acid) for Cardiac Tissue Engineering, Florence Flaig, Hélène Ragot, Alexandre Simon, Gaëlle Revet, Maria Kitsara, Lisa Kitasato, Anne Hébraud, Onnik Agbulut, Guy Schlatter, ACS Biomater Sci Eng, 2020, 6(4):2388-2400 https://doi.org/10.1021/acsbiomaterials.0c00243

[Fiamingo, 2016] Chitosan Hydrogels for the Regeneration of Infarcted Myocardium: Preparation, Physicochemical Characterization, and Biological Evaluation, Anderson Fiamingo, Alexandra Montembault , Solène-Emmanuelle Boitard, Hany Naemetalla, Onnik Agbulut, Thierry Delair, Sérgio Paulo Campana-Filho, Philippe Menasché, Laurent David. Biomacromolecules, 17(5), 2016, 1662-72 https://doi.org/10.1021/acs.biomac.6b00075

[Domengé, 2021] Efficacy of epicardial implantation of acellular chitosan hydrogels in ischemic and nonischemic heart failure: impact of the acetylation degree of chitosan, Orianne Domengé, Hélène Ragot, Robin Deloux, Agnès Crépet, Gaëlle Revet, Solène Emmanuelle Boitard , Alexandre Simon, Nathalie Mougenot, Laurent David, Thierry Delair, Alexandra Montembault, Onnik Agbulut, Acta Biomater, 2021, 119:125-139, PMID: 33161185 https://doi.org/10.1016/j.actbio.2020.10.045

[Joanne, 2016] Nanofibrous clinical-grade collagen scaffolds seeded with human cardiomyocytes induces cardiac remodeling in dilated cardiomyopathy, Pierre Joanne, Maria Kitsara, Solène-Emmanuelle Boitard, Hany Naemetalla, Valérie Vanneaux, Mathieu Pernot, Jérôme Larghero, Patricia Forest, Yong Chen, Philippe Menasché, Onnik Agbulut, Biomaterials, 2016, 80:157-168, PMID: 26708641 https://doi.org/10.1016/j.biomaterials.2015.11.035

[Alexander, 2017] Water contact angle is not a good predictor of biological responses to materials, Morgan R. Alexander, Biointerphases, Volume 12, Issue 2 (2017) https://doi.org/10.1116/1.4989843

[Dufour, 2021] Cold plasma treatment of seeds: deciphering the role of contact surfaces through multiple exposures, randomizing and stirring, T. Dufour, Q. Gutierrez, J. Phys. D: Appl. Phys., 54, 505202 (16pp), 2021 https://doi.org/10.1088/1361-6463/ac25af

[Kitsara, 2017] Fibers for hearts: A critical review on electrospinning for cardiac tissue engineering, Maria Kitsara, Onnik Agbulut, Dimitrios Kontziampasis, Yong Chen, Philippe Menasché, Acta Biomater, 48:20-40, 2017, PMID: 27826001 https://doi.org/10.1016/j.actbio.2016.11.014

[Kitsara, 2015] Fabrication of cardiac patch by using electrospun collagen fibers, Maria Kitsara, Pierre Joanne, Solène Emmanuelle Boitard, Ibtihel Ben Dhiab, Barbara Poinard, Philippe Menasché, Christian Gagnieu, Patricia Forest, Onnik Agbulut, Yong Chen, Microelectronic Engineering, Volume 144, 2015, 46-50
https://doi.org/10.1016/j.mee.2015.02.034

[Camman, 2021] 3D models of dilated cardiomyopathy: Shaping the chemical, physical and topographical properties of biomaterials to mimic the cardiac extracellular matrix, Marie Camman, Pierre Joanne, Onnik Agbulut, Christophe Hélary, Bioact Mater., 7:275-291, 2021, PMID: 34466733 https://doi.org/10.1016/j.bioactmat.2021.05.040

[Kitsara, 2022] Polysaccharide-Protein Multilayers Based on Chitosan-Fibrinogen Assemblies for Cardiac Cell Engineering, Maria Kitsara, George Tassis, Aristeidis Papagiannopoulos, Alexandre Simon, Onnik Agbulut, Stergios Pispas, Macromol Biosci., 22(1):e2100346, 2022, PMID:34648684 https://doi.org/10.1002/mabi.202100346

Supplementary material

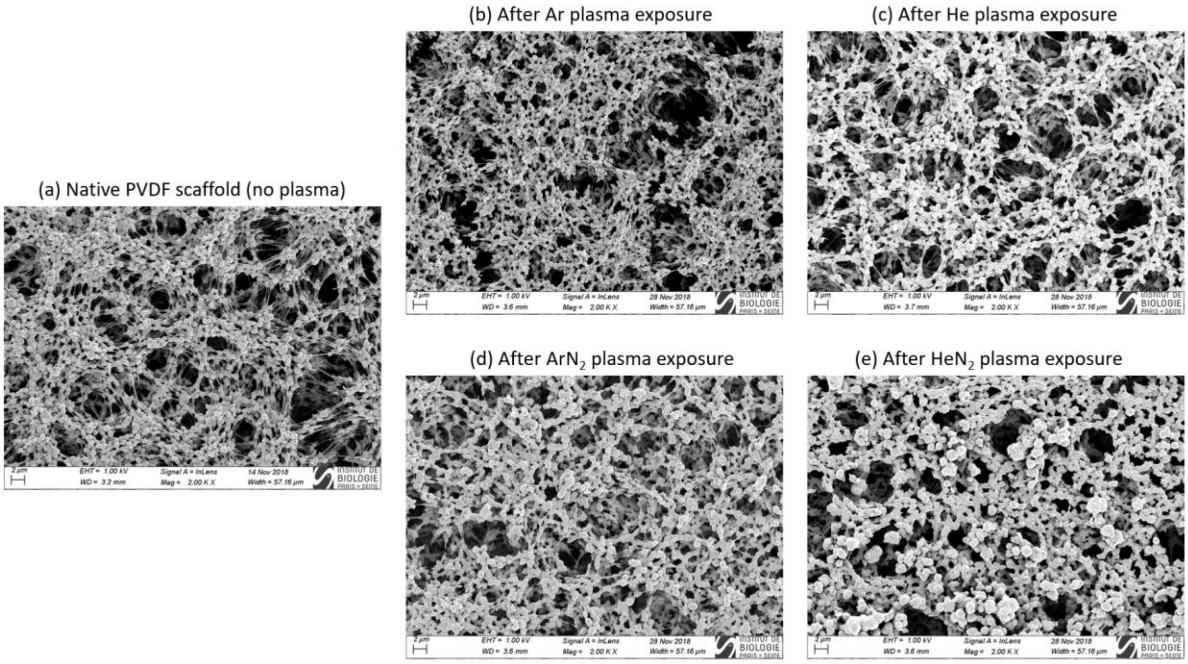

(a) Native PVDF scaffold (no plasma)

(b) After Ar plasma exposure

(c) After He plasma exposure

(d) After ArN_2 plasma exposure

(e) After HeN_2 plasma exposure

Figure 9. Scanning electron microscope (SEM) images of drop-cast scaffolds*: (a) Native PVDF scaffold obtained by 5% w/v solution, (b) PVDF scaffold after Ar plasma exposure, (c) PVDF scaffold after He plasma exposure, (d) PVDF scaffold after ArN_2 plasma exposure, (e) PVDF scaffold after HeN_2 plasma exposure. The images (b), (c), (d) and (e) correspond to the side exposed to plasma.*